第 41 卷 第 12 期 焊 接 学 报 Vol. 41(12):44 − 48
2020 年 12 月 TRANSACTIONS OF THE CHINA WELDING INSTITUTION December 2020

高氮奥氏体焊丝焊接超高强钢接头组织和性能

杨东青， 熊涵英， 黄勇， 彭勇， 王克鸿
(南京理工大学, 受控电弧智能增材技术工信部重点实验室, 南京, 210094)

摘要: 为解决超高强钢焊接冷裂纹问题, 采用强度低于母材的高氮奥氏体丝材进行 GMAW 工艺试验, 研究在不同坡口角度下超高强钢焊接接头组织性能. 结果表明, 采用该焊丝获得的接头焊缝成形良好, 焊缝截面未见裂纹缺陷. 熔合线附近组织主要为针状和板条状马氏体, 焊缝组织主要为奥氏体及被奥氏体基体所包围的铁素体树枝晶. 熔合线附近马氏体区硬度平均值为 530 HV; 焊缝区硬度平均值为 275 HV. 相对于 60°坡口接头, 90°坡口接头熔合线附近马氏体组织硬度更高. 90°坡口接头的抗拉强度平均达到 850 MPa, 最高达 887 MPa, 而 60°坡口接头抗拉强度平均仅为 690 MPa.

关键词: 超高强钢; 高氮奥氏体焊丝; 组织; 性能
中图分类号: TG 441.7 **文献标识码:** A **doi:** 10.12073/j.hjxb.20200830001

0 序言

NiCrMoV 低合金钢作为一种超高强钢, 综合性能良好, 在船舶、压力容器等领域应用广泛[1-2]. 但由于此类高强钢具有较大的淬硬倾向, 焊接时容易产生冷裂纹. 且随着强度的提高, 其焊接冷裂敏感性就越大, 还易导致焊接接头脆化[3-5].

对于 NiCrMoV 低合金高强钢焊接, 除了采用预热措施之外, 往往采用奥氏体焊材低强匹配接头抑制冷裂纹的产生, 但是会大幅降低高强钢接头强度. 现有的奥氏体焊丝如 316L 或 304 不锈钢焊材, 得到的焊缝接头强度仅为 500 ~ 600 MPa. 因此采用高强度奥氏体焊材焊接超高强钢意义重大. 李大用等人[6] 采用高铬镍奥氏体焊丝焊接低合金高强钢, 其中氮含量约为 0.1%, 焊缝主要由树枝状奥氏体组成, 无裂纹, 接头强度可达 800 MPa. 在抑制裂纹的同时可保证强度.

在奥氏体不锈钢体系中, 高氮钢以氮部分或全部代替镍合金而形成固溶强化的奥氏体不锈钢, 强度可达 1 000 MPa[7]. 因此文中拟采用高氮奥氏体焊丝作为填充材料进行超高强钢熔化极气体保护焊 (gas metal arc welding, GMAW). 目前对于此类焊丝 GMAW 工艺研究较少. 针对 8 mm 厚超高强钢板对接, 初步探索了利用高氮钢焊丝 GMAW 工艺, 分析在 60°和 90°不同的坡口角度下接头组织和力学性能, 为超高强钢焊接提供了新思路.

1 试验方法

试验使用直径 1.0 mm 的高氮奥氏体钢焊丝作为填充材料, 超高强钢板为母材, 试板尺寸 300 mm × 200 mm × 8 mm. 所用焊丝和母材成分如表 1 所示.

表 1 焊丝与母材化学元素组成 (质量分数, %)
Table 1 Chemical component of wire and substrate

材料	C	Ni	Cr	Mo	Mn	Si	N
焊丝	0.071	2.32	21.59	1.21	16.95	—	0.79
母材	0.32	1.8	1.0	0.7	1.2	0.4	—

采用 CMT + P 焊接模式,先正面焊一道, 然后背部清根, 反面焊一道. 工艺参数为正面送丝速

收稿日期: 2020 − 08 − 30
基金项目: 国家自然科学基金资助项目 (51805266); 江苏省自然科学基金青年基金 (BK20200497).

度 10 m/min，反面送丝速度 9.5 m/min，焊接速度 4 mm/s. 保护气体为 93.5% Ar + 1.5% O_2 + 5% N_2，气体流量 20 L/min. 坡口形式分别为 60°和 90°坡口，上下深度比为 5∶3. 考虑到焊枪的可达性及减少侧壁未熔合，间隙为 3 mm. 拉伸试件按国家标准 GBT 2651—2008《焊接接头拉伸试验方法》加工.

2　试验结果分析

2.1　焊缝宏观形貌

图 1 是超高强钢高氮奥氏体焊丝熔化极电弧焊接的焊缝宏观形貌和接头纵向截面宏观形貌. 接头成形良好，焊材与母材之间形成冶金结合，接头纵向截面未见气孔、裂纹等缺陷.

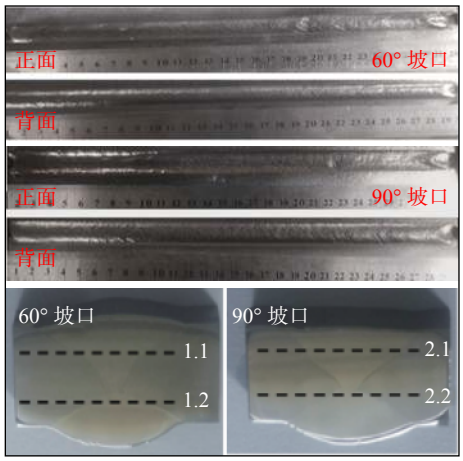

图 1　焊接接头宏观形貌

Fig. 1　Macro-graph of welded joints

2.2　显微组织分析

图 2 ~ 图 4 为不同坡口焊缝与热影响区组织形貌. 热影响区可分为明显的粗晶区和细晶区，均为马氏体组织，如图 2a, 2b, 3a, 3b 所示，对硬度影响较大. 焊缝的组织主要是被奥氏体基体所包围的铁素体树枝晶，且铁素体枝晶很密集. 除此之外，在枝晶中间还有一些“粒状”铁素体散乱的分布在整个金相中，被奥氏体基体所包围，如图 2c, 3c 所示. 两种坡口的焊缝金属和母材金属在结合处的“白亮带”区域有着明显的模糊状态，有相互渗透的现象，并观察到该区是奥氏体与马氏体的混合组织，如图 4 所示.

两种坡口接头熔合线附近热影响区组织和焊缝组织基本一致. 不同的是，90°坡口焊缝附近热影响区马氏体组织较 60°的更细小，同时 90°坡口热影响区马氏体和奥氏体的混合组织区的范围比 60°的小. 在相同的热输入参数下 90°坡口相比 60°坡口，不仅能让电弧充分达到焊缝底部，且在相同的深度下，90°坡口与电弧的接触面积更大，熔池凝固快. 60°坡口情况则相反，熔池存在时间更长，这个过程提供了晶粒继续长大的条件，因此 60°坡口热影响区马氏体和奥氏体混合组织区较 90°的大，相应的马氏体组织也较为粗大. 同时，60°坡口焊缝区也受到影响，组织相对粗大.

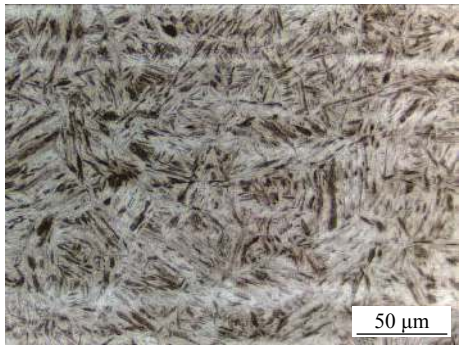

(a) 60° 坡口 HAZ 马氏体粗晶组织

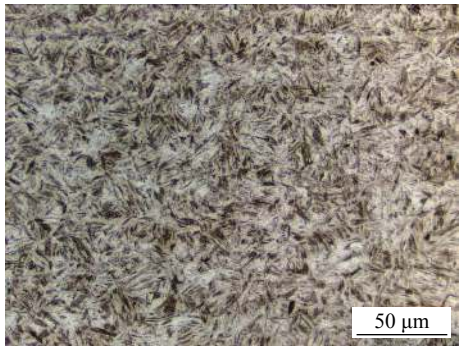

(b) 60° 坡口 HAZ 马氏体细晶组织

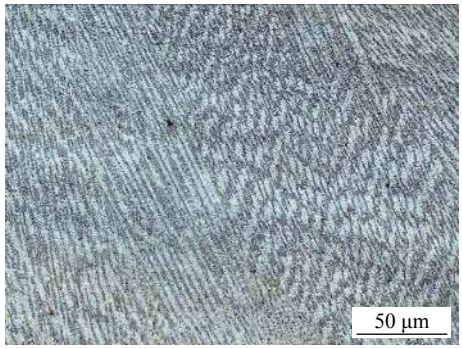

(c) 60° 坡口焊缝奥氏体组织

图 2　60°坡口不同区域显微组织

Fig. 2　Microstructure of different position with groove of 60°. (a) martensite coarse crystal structure of 60°; (b) martensite fine crystal structure of 60°; (c) weld austenite structure of 60°

如图 5 所示，在 200 ~ 240 μm 的热影响区到焊

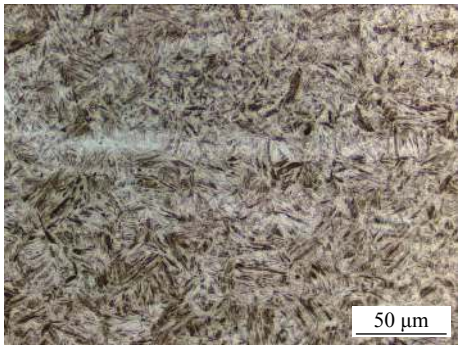

(a) 90° 坡口 HAZ 马氏体粗晶组织

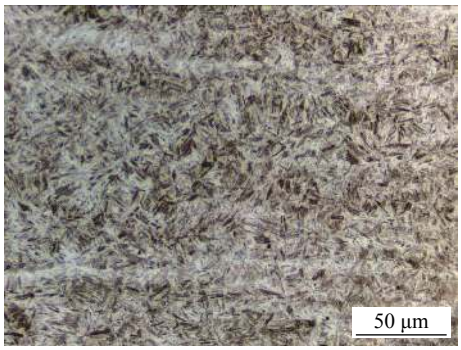

(b) 90° 坡口 HAZ 马氏体细晶组织

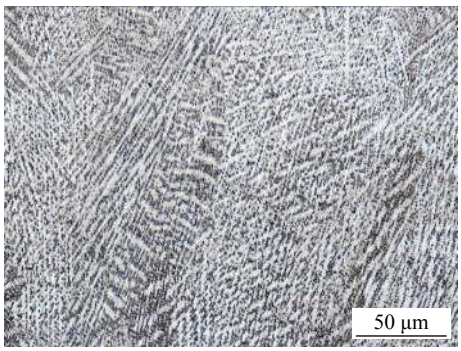

(c) 90° 坡口焊缝奥氏体组织

图 3 90°坡口不同区域显微组织

Fig. 3 Microstructure of different position with groove of 90°. (a) martensite coarse crystal structure of 90°; (b) martensite fine crystal structure of 90°; (c) weld austenite structure of 90°

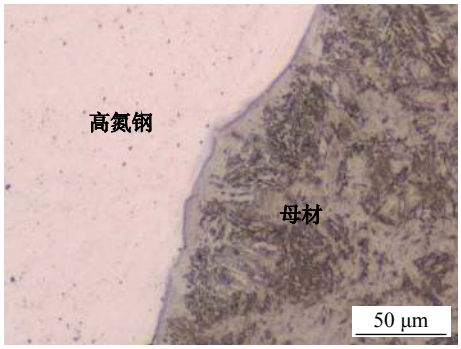

(a) 60° 坡口熔合线附近组织

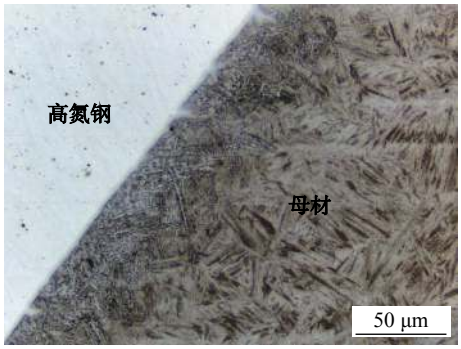

(b) 90° 坡口熔合线附近组织

图 4 熔合线区域显微组织

Fig. 4 Microstructure of fusion line. (a) 60°; (b) 90°

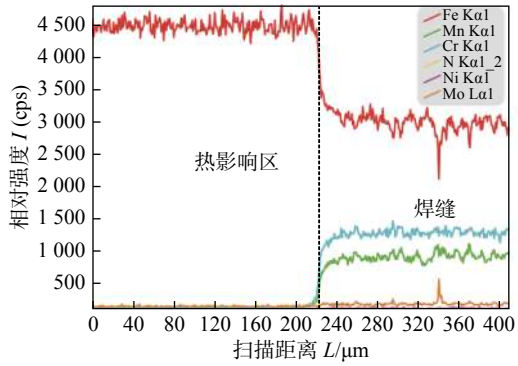

图 5 90°坡口热影响区到焊缝的元素线扫描

Fig. 5 Line scan diagram from heat affected zone to weld

缝的过渡区, 核心元素都有一个线性变化的过程, 过渡区的存在说明焊缝金属和母材金属有着充分的冶金结合. 但如图 4 所示, 90°坡口的渗透区域相对 60°坡口的更大, 且相对更均匀.

2.3 显微硬度

如图 6 所示 1 和 2 分别为 60°坡口和 90°坡口的硬度分布, 硬度取样区域线见图 1, 两种硬度分布是一致的. 硬度按从母材-热影响区-焊缝的顺序依次测量, 经过的组织依次为母材马氏体组织-马氏体细晶组织-混合组织-奥氏体组织. 根据图 6 各组试样的横向硬度分布可知, 硬度最高区域主要集中在 2.5 ~ 4 mm 和 7.5 ~ 9 mm 的区域内, 该区域的维氏硬度在 450 ~ 590 HV 之间, 60°坡口该区硬度平均值为 508 HV, 90°坡口该区硬度平均值为 536 HV. 在硬度显微镜下观测该硬度较高的区域主要为马氏体细晶区. 其中马氏体细晶区的硬度值均在 500 HV 及以上, 平均可达 530 HV; 在热影响区到焊缝区的过渡区 (3.5 ~ 4 mm), 该区组织硬度相对马氏体细晶区有一个下降过程, 主要是因为该区是马氏体组织和奥氏体组织的混合组织, 该区组织相对不均匀, 所以该区域的硬度有个下降过程. 由图 6 可知, 硬度最低的区域主要为 4.5 ~ 7 mm 区域, 均在 300 HV

以下, 平均硬度仅在 275 HV 左右. 该区域是焊缝区, 其组织主要以奥氏体为基体的树枝状铁素体晶粒组织, 故硬度较低, 两种坡口在该区硬度值相差不大.

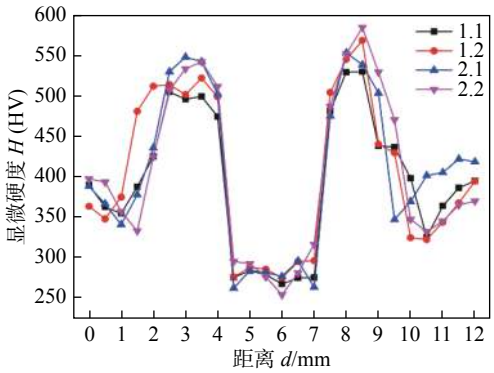

图 6　焊接接头横截面显微硬度.
Fig. 6　Micro-hardness of welded joints on cross sections

2.4　拉伸试验

从图 7 可以看出, 60°坡口试样主要是从焊缝位置断裂, 部分沿熔合线附近位置断裂, 90°坡口试样主要沿熔合线附近位置断裂. 每个试样均有颈缩现象发生. 如表 2 所示, 采用高氮奥氏体钢焊丝获得的接头平均抗拉强度可达 850 MPa, 该强度是在 90°坡口下获得的. 60°坡口接头的抗拉强度则与之相差较大, 仅为 690 MPa. 对于不同坡口接头的拉伸力学性能变化与微观组织的某些区域的大小以及晶粒的大小有关. 在相同的坡口深度下, 60°坡口侧壁与电弧的接触面积更小, 其熔池存在时间更长, 该过程为焊缝组织晶粒继续长大提供了条件, 因此 60°坡口焊缝区组织晶粒更粗大, 其拉伸性能较低. 对于 90°坡口其与电弧的接触面积更大, 其熔池凝固快, 晶粒相对较小, 因此强度更高, 并且由于混合组织区较宽, 该区域成分介于母材和焊丝之间, 得到的性能相对较低, 所以 90°坡口多断在此处.

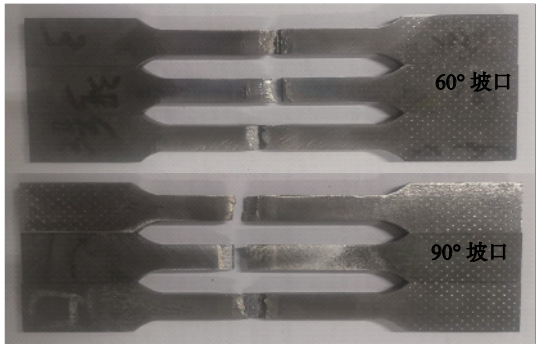

图 7　断裂后拉伸试样
Fig. 7　Fractured tensile samples

表 2　接头抗拉强度 (MPa)
Table 2　Tensile strength of joint

坡口角度	试样1	试样2	试样3	平均抗拉强度
60°	720	678	672	690
90°	887	834	829	850

3　结论

(1) 采用高氮奥氏体丝材进行超高强钢 GMAW 工艺, 可以获得成形良好的焊接接头.

(2) 高氮钢焊缝金属和超高强钢母材金属在接头熔合线处有着明显的“白亮带”存在, 有相互渗透的现象, 说明焊材和母材有着充分的冶金结合.

(3) 采用上述工艺中 60°坡口进行焊接, 接头热影响区马氏体组织晶粒较大, 且马氏体、奥氏体混合组织过渡区小; 而 90°坡口焊接接头热影响区马氏体组织晶粒更细小, 且马氏体、奥氏体混合组织过渡区较大.

(4) 采用高氮奥氏体焊丝进行 GMAW 焊接, 90°坡口可获得接头抗拉强度 (850 MPa) 高于 60°坡口接头抗拉强度 (690 MPa). 90°坡口试样马氏体细晶区硬度平均值为 536 HV, 高于 60°坡口试样 (508 HV).

参考文献

[1] 成应晋, 刘海涛, 杜义, 等. 基于插销试验的 10Ni8CrMoV 钢焊接冷裂纹敏感性分析 [J]. 材料开发与应用, 2016, 31(5): 13 − 18.
Cheng Yingjin, Liu Haitao, Du Yi, *et al*. Analysis of 10Ni8CrMoV steel welding cold cracking susceptibility on the basis of implant test[J]. Material Development and Application, 2016, 31(5): 13 − 18.

[2] 管彦朋, 李亚江, 王娟. 1 000 MPa 及以上级高强钢焊接性研究现状 [J]. 机械制造文摘(焊接分册), 2015(3): 30 − 34.
Guan Yanpeng, Li Yajiang, Wang Juan. Present situation of the study on the weldability of 1 000 MPa and above high strength low alloy steel[J]. Welding Digest of Machinery Manufacturing (Welding Volume), 2015(3): 30 − 34.

[3] 雷爱娣, 王立军, 蔡庆伍. 1 500 MPa 级低合金超高强钢微观组织与力学性能 [J]. 金属学报, 2010, 46(6): 687 − 694.
Lei Aidi, Wang Lijun, Cai Qingwu. Microstructure and mechanical properties of 1 500 MPa grade ultar-high strength low alloy steel[J]. Acta Metallurgica Sinica, 2010, 46(6): 687 − 694.

[4] Berdnikova O, Pozniakov V, Alekseienko T, *et al*. Effect of the

structure on the mechanical properties and cracking resistance of welded joints of low-alloyed high-strength steels[J]. Procedia Structural Integrity, 2019, 16: 89 − 96.

[5] 滕彬, 李小宇, 雷振, 等. 低合金高强钢激光-电弧复合热源焊接冷裂纹敏感性分析 [J]. 焊接学报, 2010, 31(11): 61 − 64.
Teng Bin, Li Xiaoyu, Lei Zhen, *et al*. Analysis on cold crack sensitivity of low alloy high strength steel weld by laser-arc hybrid welding[J]. Transactions of the China Welding Institution, 2010, 31(11): 61 − 64.

[6] 李大用, 杨东青, 王苹, 等. 高铬镍奥氏体焊丝焊接 10Ni5CrMoV 钢接头组织性能分析 [J]. 焊接学报, 2017, 38(5): 87 − 91.
Li Dayong, Yang Dongqing, Wang Pin, *et al*. Analysis of microstructure and performance of 10Ni5CrMoV steel joint welded by high chromium nickel austenitic wire[J]. Transactions of the China Welding Institution, 2017, 38(5): 87 − 91.

[7] 赵琳, 田志凌, 彭云, 等. 1Cr22Mn16N 高氮钢激光焊接 I. 焊接保护气体组成和热输入对焊缝氮含量及气孔性的影响 [J]. 焊接学报, 2007, 28(8): 89 − 91.
Zhao Lin, Tian Zhiling, Peng Yun, *et al*. Laser welding of 1Cr22Mn16N high nitrogen steel I. Influence of shielding gas composition and heat input on N-content and porosity of weld metal[J]. Transactions of the China Welding Institution, 2007, 28(8): 89 − 91.

第一作者简介: 杨东青, 1990 年出生, 博士, 讲师; 主要从事电弧增材方面的研究工作; 发表文章 10 余篇; Email: yangdq@njust.edu.cn.

通信作者简介: 黄勇, 博士, 讲师; Email: hy08161501@163.com.

（编辑： 郑红）

[上接第 32 页]

[11] Shao Q, Xu T, Yoshino T, *et al*. Multi-objective optimization of gas metal arc welding parameters and sequences for low carbon steel (S355J2G3) T-joints[J]. Journal of Iron and Steel Research, International, 2017, 24(5): 544 − 555.

[12] Goldak J, Aditya C, Malcolm B. New finite element model for welding heat sources[J]. Metallurgical and Materials Transactions B, 1984, 15B(2): 299 − 305.

[13] 徐涛, 修航, 刘东凯, 等. 焊接模拟中自适应高温截断技术及阈值优化研究 [J]. 焊接学报, 2015, 36(6): 81 − 84.
Xu Tao, Xiu Hang, Liu Dongkai, *et al*. Research on self-adaption cut-off temperature technique and threshold optimization in welding numerical simulation[J]. Transactions of the China Welding Institution, 2015, 36(6): 81 − 84.

[14] Montgomery D C. Design and analysis of experiments[M]. 5th ed. New York: John Wiley & Sons, 2001.

[15] 赵利华. 机车构架侧梁焊接数值仿真与变形控制 [D]. 成都: 西南交通大学, 2012.
Zhao Lihua. Numerical simulation and deformation control for the side bean welding of the locomotive bogie frame[D].Chengdu: Southwest Jiaotong University, 2012.

第一作者简介: 邵晴, 1990 年出生, 博士, 高级工程师; 主要研究方向为焊接结构优化及工艺优化; Email: shaoqing.ck@crrcgc.cc.

（编辑： 李帅）

Effect of element Nb on microstructures and impact toughness of CGHAZ in TiNbV micro-alloyed steels

YAN Han[1,3], ZHAO Di[1], QI Tongfu[1], LENG Xuesong[2], FU Kuijun[2], HU Fengya[2] (1. State Key Laboratory of Advanced Welding and Joining, Harbin Institute of Technology, Harbin, 150001, China; 2. State Key Laboratory of Metal Materials for Marine Equipment and Application, Iron & Steel Research Institute of Ansteel Group Corporation, Anshan, 114009, China; 3. Department of Mechanical Engineering, The University of Sheffield, Sheffield, S10 2TN, UK). pp 33-37

Abstract: The microstructure evolution and impact toughness of the coarse grain heat-affected-zone (CGHAZ) of TiNbV micro-alloyed steel were investigated by the simulated welding thermal cycle. The microstructure and grain size of the simulated CGHAZ between low-niobium steel and high-niobium steel is significantly different. When the Nb content is low (0.005%), the CGHAZ consists of ferrite, acicular ferrite, and pearlite. The ratio of the large-angle grain boundary and the small-angle grain boundary is equal, and the grain size of the CGHAZ is coarse and uneven. With the increase of Nb content, the number of grains in the high-angle grain boundary increases, and the grains are refined. However, the formation of acicular ferrite is suppressed, and the bainite content of CGHAZ increases. The formation of bainite in the micro-alloyed steel plays a leading role in the decrease of the impact toughness of CGHAZ. The content of element Nb should be controlled within an appropriate range (~ 0.02%) to obtain good impact toughness.

Key words: TiNbV micro-alloyed steel; coarse grain heat-affected-zone; element Nb; microstructure; impact toughness

Rapid evaluation of fatigue limit of AZ31B magnesium alloy joints based on energy dissipation

GUO Shaofei[1], LIU Xuesong[1], ZHANG Hongxia[2], YAN Zhifeng[2], FANG hongyuan[1] (1. State Key Laboratory of Advanced Welding and Joining, Harbin Institute of Technology, Harbin, 150001, China; 2. Taiyuan University of Technology, Taiyuan, 030024, China). pp 38-43

Abstract: The temperature rise of the material during the fatigue process is mainly caused by energy dissipation, which can be used to evaluate the fatigue performance of materials or components. However, changes in the thermal boundary conditions during the test is likely to make the evaluation result unreliable. In this paper, the fatigue performance of AZ31B magnesium alloy manual TIG welded joint was evaluated by using the temperature rise caused by energy dissipation. In order to overcome the adverse effects of changes in boundary conditions, based on the superposition principle of boundary value problem of linear partial differential equation, this paper proposes to divide the raw temperature data measured by infrared camera into two parts: temperature rise caused by boundary conditions and temperature rise caused by energy dissipation. On this basis, it is further proposed that the temperature rise caused by energy dissipation can be used to evaluate fatigue performance. Moreover, a temperature data processing method was given according to the proposed theory. The results showed that, based on the processed temperature data, the fatigue limit of the ground flush joint and the as-welded joint are 58.85 and 62.61 MPa respectively by the classical energy dissipation method (Risitano method), whose errors relative to the fatigue limit obtained by the *S-N* curve (2×10^6) are −11.82% and −0.03%, respectively.

Key words: fatigue limit; energy dissipation; magnesium alloy; experimental mechanics

Microstructure and properties of ultra-high strength steel joints welded with high nitrogen austenite wire

YANG Dongqing, XIONG Hanying, HUANG Yong, PENG Yong, WANG Kehong (Key Laboratory of Controlled Arc Intelligent Additive Manufacturing Technology, Ministry of Industry and Information Technology, Nanjing, 210094, China). pp 44-48

Abstract: In order to solve the problem of cold cracks in ultra-high-strength steel welding, the GMAW process experiment was carried out with high-nitrogen austenitic wire with lower strength than the base metal to study the microstructure and properties of ultra-high-strength steel welded joints at different grooved angles. The results show that welded joints are well formed without cracks according to cross-section of weld, the microstructure near the fusion line is mainly acicular and lath martensite, and the weld structure is mainly austenite and ferrite dendrites surrounded by austenite matrix; the average hardness of the martensite zone near the fusion line is 530 HV; the average hardness of the weld zone is

275 HV; compared to 60° grooved joints, the hardness of the martensite structure near the fusion line of 90° grooved joints are higher; The average tensile strength reaches 850 MPa, and the highest is 887 MPa, while the average tensile strength of 60° groove joints is only 690 MPa.

Key words: ultra-high strength steel; high nitrogen austenitic wire; microstructure; mechanical properties

Adaptive edge detection of molten pool based on coarse-grained regularization in restricted solution space LIU Tianyuan, BAO Jinsong, WANG Junliang, ZHENG Xiaohu, WANG Jiacheng (College of Mechanical Engineering, Donghua University, Shanghai 201600, China). pp 49-54

Abstract: Edge detection is a key step in the image processing of the molten pool. In view of the sharp changes in the arc in the molten pool area, the edge detection method that relies on artificially setting the threshold is difficult to adapt to the dynamic change of the arc. This paper proposes a deep learning-based edge extraction mode of the molten pool. Firstly, pixel-level annotation and data augmentation are performed on the original molten pool image to build a dataset. Secondly, a coarse-grained regularization method in restricted solution space (CGRRSS) is proposed to enhance edge features. Finally, the proposed method is compared with the traditional methods in both quantitative and qualitative aspects. The results show that the proposed method has a higher recall of edge points, the obtained molten pool edge is more continuous and has a better suppression effect on false edges. The detection time of a single image is 6.2 ms, which can meet the needs of online monitoring.

Key words: molten pool image; deep learning; edge detection; regularization; coarse-grained

Study on creep damage evolution of braze sealant of solid oxide fuel cell by small punch test SONG Ming, MA Shuai, DU Chuansheng, WANG Bingying, JIANG Wenchun (China University of Petroleum (East China), Qingdao, 266580, China). pp 55-60

Abstract: Obtaining the creep properties of sandwich structure of brazed joint has always been a challenge. Based on Wen-Tu creep-ductility exhaustion model, a subroutine for creep damage evolution of braze sealant of solid oxide fuel cell (SOFC) was developed in the finite element model of small punch test (SPT) using ABAQUS software. The evolution and characteristics of creep damage of the brazed joint with 304 stainless steel as base metal were studied by combining experiment and finite element analysis. The relationship between the change rate of central creep deflection and the creep strain rate of the brazed joint under different loads was obtained. The evolution of creep damage and crack propagation of brazed joint in the small punch creep test is clarified. The results show that the main fracture mode of brazed joint under multiaxial stress is brittle fracture, and the creep crack originates at the lower surface of base metal, which is 0.85 mm far away from the center of SPT specimen, and gradually propagates to the upper surface of base metal and the lower surface of the solder layer until fractures.

Key words: brazed joint; creep damage; finite element method; crack propagation; small punch test

Application of selective anodic bonding technology in grating gyroscope HAO Feifan[1,2], LI Mengwei[1,2], WANG Junqiang[1,2], JIN Li[1,2], GENG Hao[1] (1. North University of China, Taiyuan 030051, China; 2. Nantong Institute of Intelligent Opto-Mechanics, North University of China, Nantong, 226000, China). pp 61-66

Abstract: Anode bonding technology is widely used in wafer-level MEMS device manufacturing and packaging. For devices with cantilever beam structure, it is easy to attract during bonding. Selective anode bonding technology is used to prevent the gyro from attracting failure during bonding. The formula of electrostatic pull-in voltage between gyro beam and glass was educed, and the relationship model between pull-in voltage and silicon structure glass gap was established. First, the gyroscope structure was made by DRIE, then the grating was made by sputtering Al/Cr on the glass substrate, and finally the anodic bonding was performed. The results showed that the bonding interface has no defects, and the conductivity of Cr and its oxides made the silicon-glass anodic bonding without electrostatic attraction. The average bonding strength was 33.94 MPa, and the bonding quality was good.

Key words: MEMS gyroscope; anodic bonding; elec-